Origin of itinerant carriers in antiferromagnetic LaFe$_{1-x}$Mo$_x$O$_3$ studied by x-ray spectroscopies

Dibya Phuyal [1,*] Soham Mukherjee,[1] S. K. Panda,[2] Somnath Jana,[1,†] Carlo U. Segre [3] Laura Simonelli,[4]
Sergei M. Butorin [1] Håkan Rensmo,[1] and Olof Karis[1]

[1]*Division of Molecular and Condensed Matter Physics, Department of Physics, Uppsala University, Box 516, SE-75121, Uppsala, Sweden*
[2]*Department of Physics, Bennett University, Greater Noida 201310, Uttar Pradesh, India*
[3]*CSRRI and Department of Physics, Illinois Institute of Technology, Chicago, Illinois 60616, USA*
[4]*CELLS-ALBA Synchrotron, E-08290 Cerdanyola del Vallés, Barcelona, Spain*

We report on the electronic structure of doped LaFeO$_3$ at the crossover from an insulating-to-metallic phase transition. Comprehensive x-ray spectroscopic methodologies are used to understand core and valence electronic structure as well as crystal structure distortions associated with the electronic transition. Despite the antiferromagnetic (AFM) ordering at room temperature, we show direct evidence of itinerant carriers at the Fermi level revealed by resonant photoemission spectroscopy (RPES) at the Mo L_3 edge. RPES data taken at the Fe L_3 edge show spectral weight near the valence band edge and significant hybridization with O $2p$ states required for AFM ordering. Resonant inelastic x-ray scattering spectra taken across Fe $L_{2,3}$ edges show electron correlation effects (U) driven by Coulomb interactions of d electrons as well as broad charge-transfer excitations for $x \geqslant 0.2$ where the compound crosses over to a metallic state. Site substitution of Fe by Mo ions in the Fe-O$_6$ octahedra enhances the separation of the two Fe-O bonds and Fe-O-Fe bonding angles relative to the orthorhombic LaFeO$_3$, but no considerable distortions are present to the overall structure. Mo ions appear to be homogeneously doped, with average valency of both metal sites monotonically decreasing with increasing Mo concentration. This insulator-to-metal phase transition with AFM stability is primarily understood through intermediate interaction strengths between correlation (U) and bandwidth (W) at the Fe site, where an estimation of this ratio is given. These results highlight the important role of extrinsic carriers in stabilizing a unique phase transition that can guide future efforts in antiferromagnetic-metal spintronics.

I. INTRODUCTION

Chemical substitution has proven to be a useful avenue to create unusual ground states in oxide materials [1,2]. Perovskite oxide compounds are known to host numerous novel ground states, such as charge ordering, orbital ordering, spin ordering, etc. [1]. The interplay between the charge, orbital, and spin degrees of freedom—tuned via chemical doping—has resulted in a wealth of interesting phenomena such as metal-insulator transitions, colossal magnetoresistance, high T_C superconductivity, multiferroicity, etc. [2–7]. These aspects make the prospect of identifying new electronic phases in oxide materials very intriguing and a focus of intense research. A common approach for the discovery of new oxide materials is through doping a host material, specifically targeted to tune between different electronic phases [3] and local

structure [8,9]. In oxide perovskites with the generic ABO$_3$ formula, the transition metal (TM) dopant (B') at the B site is often used as a design principle to stabilize carriers from an insulating to a metallic ground state [10]. These complex transitions, described in the Zaanen-Sawatsky-Allen scheme [11], are typically characterized by the relative strengths of the on-site Coulomb correlation energy (U), bandwidth (W) of the d shell of the transition metal, and the hybridization strength between the TM $3d$ and O $2p$ states (t_{pd}). The competition between localization due to on-site Coulomb correlations between electrons and the kinetic energy gain due to band formation lies at the heart of the diverse electronic and magnetic properties of transition metal oxides.

In a previous study, a metalliclike behavior was reported for the insulating LaFeO$_3$ (LFO) when doped with Mo ions [12]. The antiferromagnetic (AFM) insulator first moves to a small gap Mott insulator by increasing the Mo doping up to 20%. At doping levels above 20%, it shows signatures of a crossover from insulating to itinerant while maintaining antiferromagnetic (AFM) order, where Fe ions also show charge disproportionation [12]. In the parent compound LaFeO$_3$, Fe sites are in the $+3$ oxidation state. The substitution of Fe at the B site by Mo ions in LaFe$_{1-x}$Mo$_x$O$_3$ (LFMO) is intimately linked to equal contributions of Fe^{2+} and Fe^{3+}, similar to that found in nickelates [13–16], and in related SrFeO$_{3-\delta}$ [17] and La$_{1/3}$Sr$_{2/3}$FeO$_3$ [18] systems. More interestingly, both

experimental and theoretical findings on a 25% Mo doping sample establish a system that shows an orbital-selective Mott state, where the metallic character at the Fermi level emerges from Mo t_{2g} states, while occupied Fe $3d$ states remain positioned several eV below the Fermi level (E_F) [12]. The electronic charge disproportionation is described by two valences at the Fe site: Fe1 (3+) and Fe2 (2+) respectively, where Fe-O bond distances are disproportionate due to nearby Mo ions but not sufficiently to drive a change in crystal structure. By increasing site substitution with Mo ions, i.e., doping extrinsic carriers, the Fe^{2+} content increases continuously until a crossover from insulator to metal transition (20% Mo) is reached. The average valence of Fe at $x = 0.20$ and $x = 0.25$ suggests an equal number of Fe^{3+} and Fe^{2+}. Further increase of Mo doping does not seem to change the Fe valence. The additional electrons lead to a measureable band with dominant Mo character. The electronic structure reported for this compound is very rich in detail, and merits further experimental information to point to competing interactions and substantiate the materials' reported physical properties.

To this purpose, we combine several x-ray spectroscopies to address the nature of the electronic structure and identify the role of correlations as well as any structural distortions as a function of doping in the $LaFe_{1-x}Mo_xO_3$ system. We investigate the effects of electron doping at three different doping levels: a parent compound ($x = 0$, $LaFeO_3$), and low ($x = 0.10$, $LaFe_{0.90}Mo_{0.10}O_3$) and high ($x = 0.25$, $LaFe_{0.75}Mo_{0.25}O_3$) doping, with the latter that is the maximum solid solubility limit in these systems. We employ resonant photoelectron spectroscopy (RPES), which provides an element-selective projection to the partial density of states (DOS) [19,20] and specifically accesses the character of d states near the Fermi level (E_F) and their hybridization with O $2p$ states. The transition from an insulating to a metallic phase is unambiguously identified through the appearance of appreciable spectral DOS at the Fermi level (E_F). The corresponding resonant inelastic x-ray scattering (RIXS) spectra, performed with excitations across the Fe L_3 edge, allow us to follow the resonant electronic excitations as a function of doping. As we progress from the insulating phase with $x \leqslant 0.15$ into the metallic phase with $x \geqslant 0.2$, excitations evolve from narrow energy loss features, characteristic of insulating systems, to broad interband excitations, that are instead characteristic of metallic samples.

Moreover, chemical speciation, including changes to average formal valency of the metal sites, degree of noncentrosymmetricity of the metal-O_6 environment, and short-range ordering of the B sites in the $LaFe_{1-x}Mo_xO_3$ system, were investigated using extended x-ray absorption fine structure (EXAFS). Our EXAFS results show that the Mo substitution at the Fe site is homogeneous. Mo doping systematically decreases the effective formal valency of both Fe and Mo ions, without destroying the centrosymmetric nature of the metal-O_6 cage. The analysis from these combined techniques reveals the origin of itinerant carriers in a unique antiferromagnetic $LaFe_{1-x}Mo_xO_3$ system. These findings not only provide insights into the origins of itinerant carriers in a magnetic system, but also point to distinctive properties of complex oxides.

II. EXPERIMENT

A. Solid-state synthesis

Polycrystalline ceramics were prepared by the solid-state synthesis procedure. Stoichiometric ratios of preheated La_2O_3, Fe_2O_3, and MoO_3 powders were thoroughly mixed and the obtained fine powder was subsequently annealed at 1200 °C in a 99% Ar/1%H_2 gas for 12 h and cooled to room temperature at 5 °C/min. X-ray diffraction (PANalytical MRD II) was used to check the phase integrity for any impurities. Finally, the powder was pressed to 5 GPa to form a 5-mm-diameter pellet and subsequently sintered for 6 h at 1200 °C in the 99% Ar/1%H_2 gas environment.

B. Photoemission and high-resolution hard x-ray absorption near edge structure

Photoelectron spectroscopy measurements were performed at the Diamond Light Source using the beamline I09 (Didcot, UK). All data were recorded at room temperature with a base pressure of 2.0×10^{-10} mbar. Both soft and hard x-ray photoelectron spectroscopies (HAXPES) were collected in resonant condition across the Fe L_3 and Mo L_3 edges, respectively. The soft x-ray energy was selected through a plane grating monochromator, whereas a Si (111) double-crystal monochromator was used for hard x-ray energies. An EW-4000 photoelectron analyzer (VG Scienta) with a slit width set to 0.2 mm was used to record spectra at normal emission. The corresponding x-ray absorption was measured in total electron yield (TEY) mode. The binding energy scale was calibrated by setting the Au $4f$ core level and E_F of a gold reference foil to 84.0 and 0.0 eV respectively. The total instrumental resolution for the PES measurements was kept below 250 meV at the selected soft and hard x-ray energies. High-resolution absorption spectra were collected at the Fe K edge at the CLÆSS beamline [21] of the ALBA Synchrotron (Barcelona, Spain). The spectra were recorded by selecting the $K\beta_{1,3}$ emission line (7058 eV) and scanning the incoming energy across the Fe K edge by means of a Si(311) double-crystal monochromator. The energy in the high-resolution fluorescence detected x-ray absorption near edge Structure (HERFD-XANES) was selected using a Si (333) dynamical bent diced analyzer crystal and an energy dispersive one-dimensional(1D) detector in Rowland circle geometry (Rowland radius = 1 m). The overall energy resolution was around 0.9 eV, full width at half maximum of the quasielastic line collected over a tape foil.

C. XES and RIXS

Fe L x-ray absorption (XAS), emission (XES), and resonant inelastic x-ray scattering (RIXS) measurements were performed at the 8.0.1 beamline at the Advanced Light Source (Berkeley, CA). The x-ray absorption spectrum was acquired in both total electron yield (TEY) and total fluorescence yield (TFY) modes. All measurements were performed at room temperature under ultrahigh-vacuum conditions (10^{-10} mbar) with the incident beam 45° to the surface. The spectra have been normalized to the beam flux measured by a gold mesh and calibrated based on a TiO_2 (anatase) standard. The XES data were energy calibrated using metallic emission lines as a
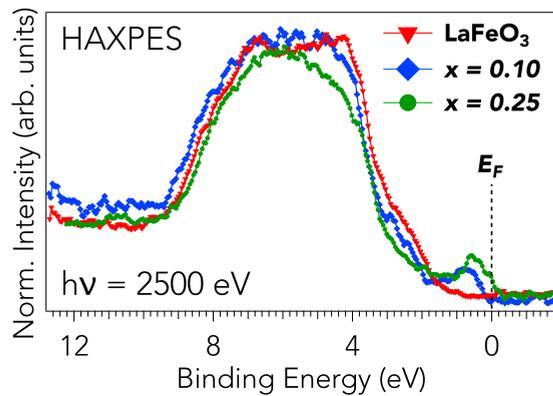
FIG. 1. HAXPES data measured at 2500 eV on the LaFe$_{1-x}$Mo$_x$O$_3$ series. Both insulating LaFeO$_3$ (red triangles) and $x = 0.10$ (blue diamond) systems exhibit gaps between the valence band and the E_F, whereas for the $x = 0.25$ composition (green circle), there is clear density of states at E_F, characteristic of a metal.

reference (Zn $L_{\alpha,\beta}$, Mn $L_{\alpha,\beta}$, Fe $L_{\alpha,\beta}$). The RIXS spectra were taken across the Fe L_3 absorption resonance energy with a total instrumental resolution of 350 meV as measured from the elastic profile [22–24].

D. Extended x-ray absorption fine structure (EXAFS)

A dual detector setup was used in simultaneous EXAFS measurements in transmission and fluorescence modes at the Fe K edge and the Mo K edge. The measurements were performed at room temperature (300 K) at the Sector 10 (MRCAT) bending magnet beamline at the Advanced Photon Source, Argonne National Laboratories (USA). For each Fe K and Mo K measurement, corresponding elemental foils were simultaneously measured to track any energy shifts in the beam during the data collection. Detailed fits to the data were carried out up to the maximum usable k values (10.0 Å^{-1} for Fe K and 12.0 Å^{-1} for Mo K) using the standard EXAFS equation with the help of the ARTEMIS program [25], which uses FEFF 6.0 code [26] to calculate the scattering amplitudes and phases for all possible scattering events. The details of the data analysis fits and results are tabulated in the Supplemental Material [27].

III. RESULTS

Figure 1 shows the HAXPES valence band measured at an incident energy of 2500 eV for LaFe$_{1-x}$Mo$_x$O$_3$ compounds ($x = 0.0, 0.10,$ and 0.25). The spectra were energy calibrated relative to Au $4f_{7/2}$ and normalized to the La $5p_{3/2}$ peak (17.7 eV). At high photon energies, the probing depth is relatively high and signatures from the surface do not dominate the spectra. A close inspection of the valence band near the Fermi level (E_F) shows an increase in spectral weight as a function of Mo content. For $x = 0$ (red curve), a sizable gap between the valence band and the E_F is clearly observable, in agreement with previous soft x-ray studies on LaFeO$_3$ [28,29]. For the $x = 0.10$ doped sample (blue curve), there is a nominal increase of states near 0.8 eV in binding energy

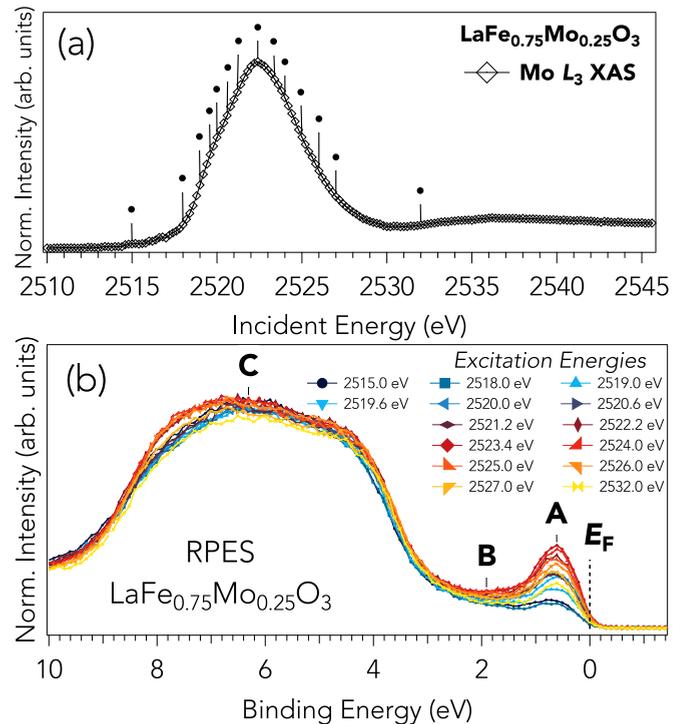FIG. 2. (a) The absorption spectrum for $x = 0.25$ measured at the Mo L_3 edge. The dots (•) indicate the excitation energies used to collect photoemission spectra. (b) RPES spectra for LaFe$_{0.75}$Mo$_{0.25}$O$_3$ showing three enhanced spectral features that relate to Mo $4d$ contribution in the valence band.

(BE). However, the tail of the valence band still terminates below E_F with negligible intensity at 0 eV, consistent with its insulating properties. For the $x = 0.25$ sample, there is a nominal increase of states near 0.5 eV, with a sizable intensity at E_F, in parallel with the transition to a metallic state.

In order to map the different spectral contributions in the valence band, resonant photoemission at the Mo L_3 edge probes the direct Mo $4d$ states. Figure 2 shows the x-ray absorption [panel (a)] and resonant photoemission spectra [panel (b)] taken across the Mo L_3 edge for the $x = 0.25$ compound. The absorption spectrum corresponds to the Mo $2p \rightarrow 4d$ transitions, in close agreement with previously reported Mo L edge spectra of Mo-based oxide perovskites [30–33]. The valence band resonant photoemission is obtained by tuning the excitation photon energy at selected energies (marked with dots) across the Mo L_3 absorption edge. The measured resonant photoemission spectra exhibit four distinct features that are enhanced when tuned to resonant excitation energies in Fig. 2(b). The spectral region around 0.5 eV BE shows an intense and narrow peak (A) that is enhanced monotonically as the excitation energy approaches the absorption maximum at 2523.5 eV, and decreases as the incident energy is tuned past the resonance condition. Feature A can be assigned to Mo $4d$ t_{2g} states [12], where the itinerant electron in the partially filled t_{2g} states gives rise to the itinerant character for $x = 0.25$. Feature B at ~2 eV BE also shows resonant behavior, particularly at the excitation energy corresponding to the absorption threshold ($h\nu = 2522.2$ eV), which points to Mo d states that lie just below the Fermi level. The $4d$
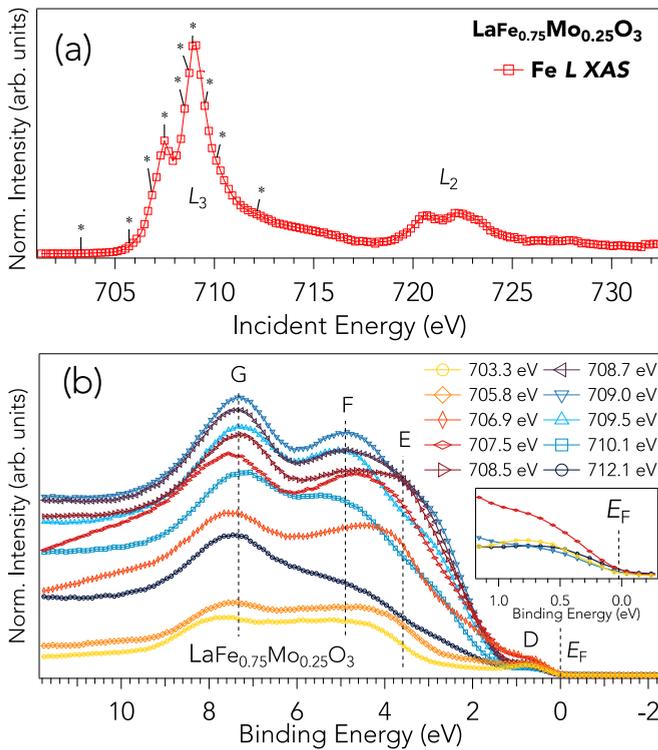
FIG. 3. (a) The Fe $L_{2,3}$ XAS spectrum for $x = 0.25$ with a strong shoulder centered at ~707.5 eV. The tick marks indicate the excitation energies used for RPES spectra. (b) RPES data collected at several incident energies with four principal structures that are enhanced as compared to the off-resonance case (703.3 eV, yellow curve). An expanded view in the inset shows features that are related to the charge disproportionated Fe states. The red curve taken at the shoulder peak is enhanced near 0.5 eV and is representative of Fe^{2+} states while the features near 3 eV are resonantly enhanced when taken at the absorption maximum.

transition metal oxides (TMOs) generally have significant bandwidths (W) and small electron correlation U due to the large spatial extent of $4d$ orbitals. The broad region between 4 and 8 eV (C) corresponds to the Mo $4d$-O $2p$ admixture as was shown by band structure calculations in our previous study [12]. The discussion here primarily pertains to resonances near E_F, and the spectra in Fig. 2(b) qualitatively show the emergence of new Mo $4d$ states and lend evidence for a delocalized character and specifically establish the metallicity in this material for doping levels at $x = 0.25$.

A similar experiment has been performed with photon energies across the Fe L_3 edge to probe the partial spectral weight of Fe $3d$ states in the valence band. The corresponding x-ray absorption spectrum collected in total electron yield (TEY) mode is shown in Fig. 3(a). The selected energies for the RPES valence band data are marked with an asterisk and corresponding RPES spectra shown in Fig. 3(b). The off-resonance condition is fixed at 703.3 eV and the on-resonance condition is determined from the peak position of the Fe L_3 XAS edge maximum. The spectrum shows a significant intensity enhancement for several features (labeled D–G) and follows a photon energy dependence. The intensity at E_F shows no measurable changes, indicating that the partial
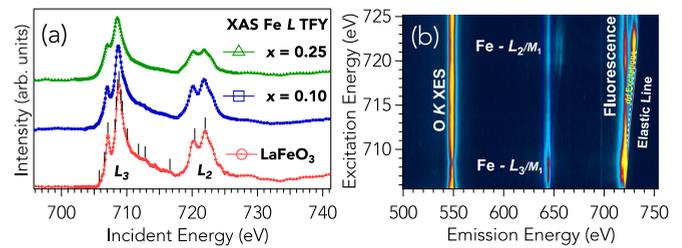

FIG. 4. (a) Fe $L_{2,3}$ XAS measured in TFY mode for $LaFeO_3$ (red), $x = 0.10$ (blue), and $x = 0.25$ (green) samples. The tick marks indicate the excitation energies used for RIXS spectra. (b) Two-dimensional RIXS intensity map measured across the entire $L_{2,3}$ edge for the $x = 0.25$ sample displayed against the excitation (vertical axis) and emission (horizontal axis) photon energy.

spectral weight at E_F has no significant contributions from Fe $3d$ states and that metallicity can be attributed solely to Mo $4d$ states, forming an impurity band. The structures towards the higher binding energy side, F and G, are dominated by the O $2p$-Fe $3d$ hybridized states. Moreover, these measurements reveal features D and E having their maximum resonant intensity at different incident energies. The inset in Fig. 3(b) shows a narrow range of the valence band expanded at a few selected energies (703.0, 707.5, 709.0, and well above resonance at 712.1 eV). When the incident energy is tuned to the maximum of the shoulder peak at 707.5 eV [Fig. 3(a)], an enhancement in feature D just below the E_F is seen (feature D, at 0.8 eV BE) and points to Fe1 t_{2g} character according to our previous calculations [12]. Conversely, at the maximum of the absorption spectrum (709.0 eV), the structure E near 3 eV gains substantial intensity in contrast to the off-resonance energy (703.3 eV) and is associated with Fe2 t_{2g} states. We argue the $x = 0.25$ compound to be a charge disproportionated system of Fe^{2+} (Fe1) and Fe^{3+} (Fe2) nominal charge states with narrow band partially filled t_{2g} states with contributions at different energy positions [12]. One set of states originates from Fe^{2+}, whose t_{2g} states are shown to lie closer to the Fermi level, and the other from Fe^{3+} whose states contribute further below E_F. Since feature D structure is enhanced at the low-energy shoulder feature in the Fe L XAS spectrum [see Fig. 3(a)], peak D can be ascribed to Fe1 and feature E to Fe2 t_{2g} states. The variations in spectral intensities at a fixed incoming energy can thus be directly linked to the different valency and charge distribution of Fe sites in the compound.

A. Fe L RIXS

RIXS can offer valuable insights into the insulating-to-metallic transition and the correlation effects within the Fe d band [22,23]. RIXS measurements were carried out by tuning the incident photon energy across the Fe L edge for the three compounds presented here. An overview of the Fe L edge XAS spectra collected in total fluorescence yield (TFY) mode is shown in Fig. 4(a). The spectral profiles are similar for all samples, as is the position of the absorption maximum at 709 eV for $LaFeO_3$ and $x = 0.10$, which gets shifted slightly to 708.5 eV for the $x = 0.25$ sample. The lower-energy shoulder peak near 707 eV is more prominent
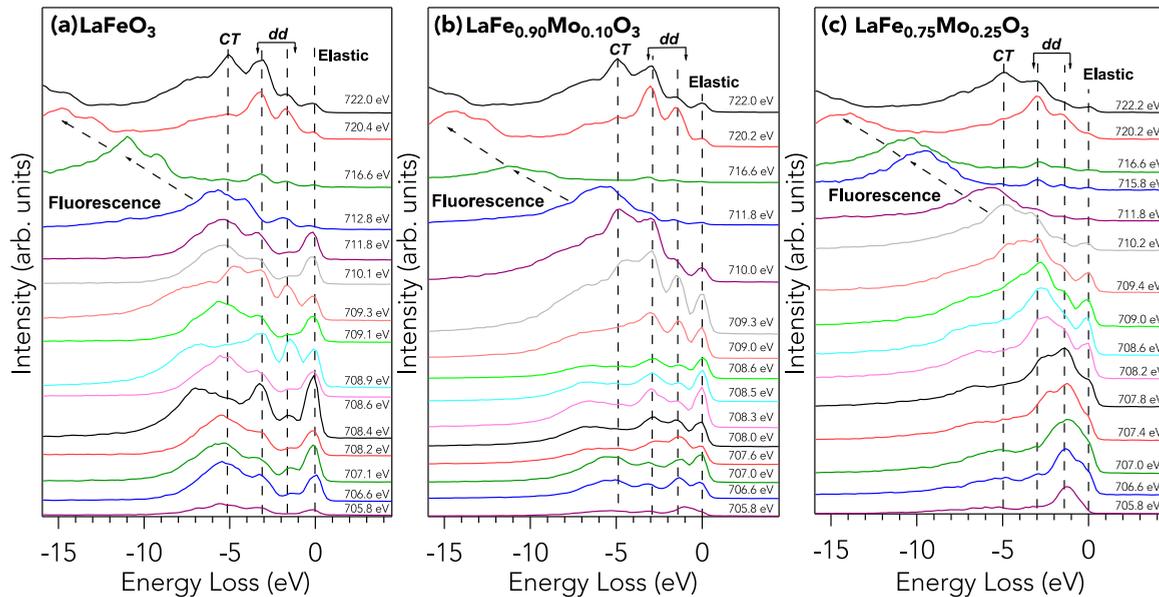
FIG. 5. Fe $L_{2,3}$ edge RIXS spectra for (a) the undoped parent LaFeO$_3$, (b) $x = 0.10$ Mo-doped sample, and (c) the metallic crossover at $x = 0.25$ at selected photon energies. The vertical dashed lines indicate energy positions of inelastic loss features and arrows are used to guide the linearly dispersing fluorescencelike structure.

for $x = 0.25$ and is attributed largely to Fe^{2+} character [12]. The full RIXS map for the $x = 0.25$ sample was taken across the Fe $L_{2,3}$ edges and is shown in Fig. 4(b). The RIXS map taken across the Fe $L_{2,3}$ edge (vertical axis) consists of three main regions. These are (from high to low emission energy) the Fe $L_{2,3}$ edge RIXS, the Fe $L_{2,3}/M_1$, and O K XES. One can see that the Fe $L_{2,3}$ edge RIXS signals consist of energy-loss features (Fe $3d$-$3d$ orbital excitations) that are parallel to the elastic line, while the "normal" fluorescence features have fixed emission energies.

Figure 5 shows the measured RIXS spectra for the $x = 0$, 0.10, and 0.25 samples measured at various photon energies across both L_3 and L_2 absorption thresholds as indicated by tick marks in Fig. 4(a). The RIXS spectra are plotted as a function of energy loss, which is defined as the difference between incident and emitted photon energies. All spectra were measured using the same acquisition time and have been normalized to the incident flux. There are several well-resolved structures that can be identified based on the energy loss of the excitations involved. First, the elastic line at 0 eV energy loss comes from the recombination of the $2p^5 3d^6$ intermediate state to recreate the ground state, $2p^6 3d^5$. Secondly, at low energy losses, both the two insulating LaFeO$_3$ [Fig. 5(a)] and $x = 0.10$ [Fig. 5(b)] samples exhibit three constant energy loss features centered around -1.6, -3.1, and -5.1 eV (indicated by dashed lines). The higher-energy loss feature at -5.1 eV is readily distinguished as a charge-transfer (CT) excitation and corresponds to O $\rightarrow$ Fe ligand-to-metal charge transfer to hybridized Fe $3d$-O $2p$ states. The two lower-energy features (<4 eV) can be assigned to intrasite Fe d-d excitations. These are typical of strongly correlated oxides and are observed in many other similar iron-based compounds [34–37]. The fixed energy loss features are assigned to electronic excitations that involve localized Fe d states. The $3d$ manifold is nominally split into t_{2g} and e_g

submanifolds that can be separated to distinct energies of the $2p$-$3d$ (t_{2g}) and $2p$-$3d(e_g)$ resonant processes. The excitations within the t_{2g} manifold will occur at a lower energy than scattering involving e_g levels, with the energy difference corresponding to the t_{2g} and e_g splitting. This allows us to assign the two d-d features for LaFeO$_3$ and $x = 0.10$ samples to intra-t_{2g} processes (-1.6 eV) and t_{2g}-e_g processes (-3.1 eV). Excitations involving delocalized character linearly disperse with incident energy ($h\nu_i$) [22,23]. Dispersing features on an energy loss scale establish their origin as fluorescentlike decay of the core hole rather than Raman-type loss features. Overall, the low- and high-energy inelastic features for both ($x = 0$ and $x = 0.10$) data sets show similar trends in energy positions in both d-d and CT excitations.

RIXS on LaFe$_{0.75}$Mo$_{0.25}$O$_3$ [Fig. 5(c)] clearly shows strong fluorescence contributions at low energy losses that are superimposed on top of the d-d excitations, which is a characteristic feature of a metallic sample [16,38], where low-energy excitations across the Fermi level are possible. Our first observation is that the spectral weight in the fluorescence features has increased relative to the spectral weight in the Raman modes for the insulating samples. Fluorescence features are already present at the onset of absorption (705.8 eV), common to metallic and semimetallic systems [39]. We also observe that at excitation energies past the L_3 edge, the CT and d-d elastic features become evident as the fluorescence structures become well separated. However, the respective measured peaks for $x = 0.25$ are broadened likely due to an increase in the bandwidth of these electronic excitations. Further support for this interpretation is provided from photoemission spectra that reveal both Fe d and Mo d states at 0.8 eV below the Fermi level [see Figs. 2(b) and F3(b)]. The similarity between the resonance behavior and energy positions of the two d-d peaks in both insulating (LaFeO$_3$ and $x = 0.10$) and metallic ($x = 0.25$) compounds strongly suggests that it has the same
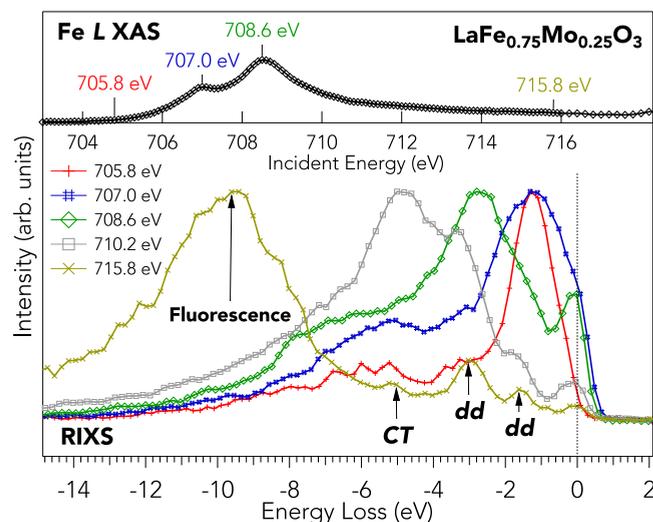
FIG. 6. RIXS spectra taken at selected excitation energies for $x = 0.25$ sample. The linearly dispersing fluorescence lines reveal several Raman features that point to strong electron-electron correlations within the Fe d manifold.

origin in both compounds, namely, a local d-d excitation that points to electronic correlation.

In order to further disentangle the origin of the observed Raman features in the $x = 0.25$ metallic sample, we closely examine its RIXS data. Since the inelastic signal at the L_3 resonance is actually a superposition of fluorescence, Raman d-d excitations, and continuum excitations across the Fermi level, we focus on a few measurements using excitation energy below, at, and above the L_3 resonance where the Raman and fluorescence components are well separated as shown in Fig. 6. The excitation energies correspond to the baseline of the XAS peak (705.8 eV), the low-energy shoulder peak that corresponds to the predominantly Fe^{2+} L_3 peak (707.0 eV), the largely Fe^{3+} site at Fe L_3 absorption maximum (708.6 eV), and well above the resonance (715.8 eV). All spectra are normalized to the intensity of the strong fluorescence peak that shifts linearly with excitation energy. The low-energy loss spectral components (<5 eV) (<5 eV) can still be tracked at higher excitation energies, as evident from the 715.8-eV spectra taken in between the L_3 and L_2 absorption edges. Furthermore, RIXS spectra for the metallic sample exhibit clear low-energy loss intensities below 1.5 eV, providing a fingerprint to closing of the insulating gap. This signature has also been observed in several insulating-to-metallic transitions such as in NdNiO$_3$ [16] and La$_{1-x}$Sr$_x$MnO$_3$ [40]. The spectra taken at 707 and 708.6 eV show a complex profile that is an amalgamation of band fluorescence, electron-hole pair continuum excitations across the Fermi level, and phenomena related to the presence of different Fe sites in the metallic phase. We rationalize this position the following way. An *intersite d-d* transition between the charge-disproportionated Fe sites can occur since both sites exist in a similar high-spin alignment ($S = 2$ for Fe^{2+} and $S = 5/2$ for Fe^{3+}) [41]. Another tangible link to the observed d-d transition can occur from the Fe-Mo intersite excitations mediated by the oxygen hybridization since the high binding energy part of
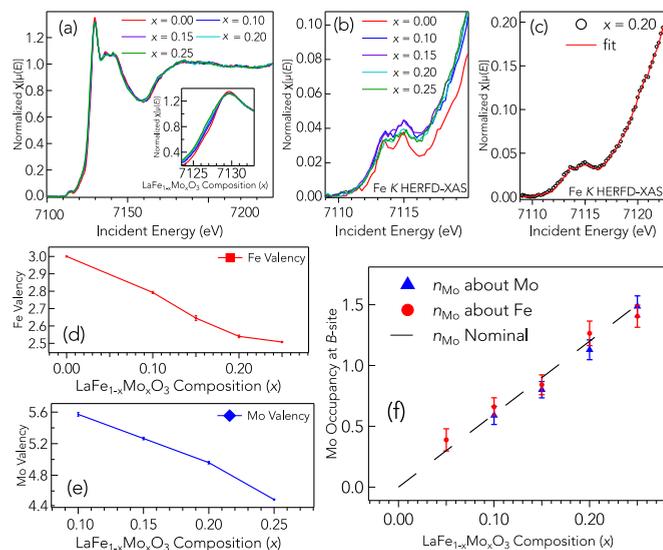

FIG. 7. (a) Normalized Fe K HERFD-XANES (300 K) for the LaFe$_{1-x}$Mo$_x$O$_3$ series; inset shows the absorption edge position systematically shifting to lower energies with increasing Mo content. (b) Enhanced preedge features. (c) Fit to the $x = 0.2$ sample. (d) Formal valence of Fe and (e) Mo decreasing with Mo doping. (f) Number of Mo ions (n_{Mo}) around each Mo (blue triangles) and Fe (red circles) site.

the valence band has contributions from both Fe $3d$ and Mo $4d$, as highlighted in the photoemission part of this study. This can lead to hybridization between the Fe d and the high binding energy part of the Mo d bands as was proposed for FeTiO$_3$ [42], TbMnO$_3$ [43], and several double-perovskite compounds [44,45]. The presence of partially filled Mo d states extends across the Fermi level to open additional pathways for the neutral charge fluctuations. The two TMs' octahedra always share one oxygen at a corresponding vertex, and thus the intersite d-d transfer can proceed via the hybridized O $2p$ states. However, calculations have to be developed to capture the full understanding of the observed data.

B. Fe K HERFD-XANES, Fe K XAFS, and Mo K XAFS

Figure 7(a) shows the normalized Fe K HERFD-XANES for the LaFe$_{1-x}$Mo$_x$O$_3$ series. With increasing Mo content, the absorption edge position systematically shifts to lower energies [inset of Fig. 7(a)], suggesting a decrease in the formal valence of Fe. Figure 7(b) shows an expanded view of the well-resolved preedge features. One can observe how the intensity of these peaks decreases going from a pure Fe^{3+} state (LaFeO$_3$, in black) to the doped compounds, which are a mixture of Fe^{3+} and Fe^{2+}. Linear combination fits to the preedge help us to quantify the ratio of Fe^{2+} and Fe^{3+} in the samples, considering $x = 0.0$ (pure Fe^{3+} state) and $x = 0.25$ (Fe^{2+}:$Fe^{3+} = 1:1$) as the end members. A representative fit of the series over -20 to -5 eV across the Fe K absorption edge of the $x = 0.2$ sample is shown Fig. 7(c). The formal valence per Fe site can then be calculated as a weighted average of the number of Fe^{2+} and Fe^{3+} ions occurring in a given composition. Figure 7(d) shows how the formal valence of Fe in the LaFe$_{1-x}$Mo$_x$O$_3$ series systematically decreases as

a function of Mo doping, suggesting an increasing number of Fe^{2+} sites, thereby shifting the Fe K absorption edge position to lower energies [inset of Fig. 7(a)]. Accounting for overall charge neutrality allows us to extract the average valency per Mo site, which also decreases with increasing Mo concentration. It is important to note here that the fit to Fe K HERFD-XANES for the $x = 0.2$ sample yields only $7\% \pm 2\%$ of the $x = 0.0$ sample (pure Fe^{3+}), suggesting the systems $x = 0.2$ and $x = 0.25$ to be quite similar, as reported previously [12]. Further electron doping can now fill up only the Mo bands, and hence a larger reduction of Mo valency for the $x = 0.25$ system in Fig. 7(e). These extra electrons at the Mo sites must be associated with the observed metallicity, as identified from our RPES and RIXS measurements.

Local structural effects such as clustering, phase segregation, and B-site ordering that can strongly influence bulk transport properties were also addressed using conventional EXAFS technique. Details of the analysis and structural parameters extracted are tabulated in the Supplemental Material [27]. The key findings are (a) Mo exists in a single environment (absence of isosbestic points in Mo K XANES), (b) Mo gets doped at Fe sites and not interstices, (c) no evidence of Mo clustering or growth of Mo-rich phases, and (d) high degree of local homogeneity. The fraction of Fe and Mo ions per B site around a Fe and Mo absorber were estimated independently and plotted in Fig. 7(f), which roughly parallels the nominal fraction estimated from global stoichiometry of the LaFe$_{1-x}$Mo$_x$O$_3$ samples.

IV. DISCUSSION

An AFM ground state generally favors more localized electrons while FM favors an itinerant [46]. The significant hybridization of the localized Fe states with O $2p$ states allows for an energy gain due to the delocalization of Mo d states. The $4d$ TMOs generally create the energy bands with significant bandwidths (W) due to the larger spatial extent of the $4d$ orbitals, thereby decreasing the overall correlation effects. An AFM state can be realized if the value of U is sufficiently small and comparable with the bandwidth [10,43]. A transition from an AFM insulator to an AFM metal is thus expected to occur as U/W is varied within this picture. The half-filled t_{2g}^3 orbitals present in the Fe^{3+} ions strongly favor the anion-mediated superexchange and lead to an AFM state. By doping, we introduce additional electrons occupying the minority spin t_{2g} states that drive the system to approach a low U limit. For the $x = 0.25$ compound, Fe ions maintain their AFM characteristics despite the presence of Mo impurity bands.

The changes to the electronic structure are not accompanied by appreciable lattice distortions, similar to that found in charge-disproportionated La$_{0.33}$Sr$_{0.67}$FeO$_3$ [45]. The bond lengths and lattice distortions to the Fe-O polyhedra, which affect the electron hopping between sites and in turn modify the size of W, vary as a result of Mo doping. By site substitution of Mo, the Fe-O-Fe bond angle increases from 163° to 175° for LaFeO$_3$ and metallic $x = 0.25$, respectively, and is shown in Fig. 8(a). This also decreases the cooperative tilting of the octahedra [Fig. 8(b)], and increases the localized d-electron
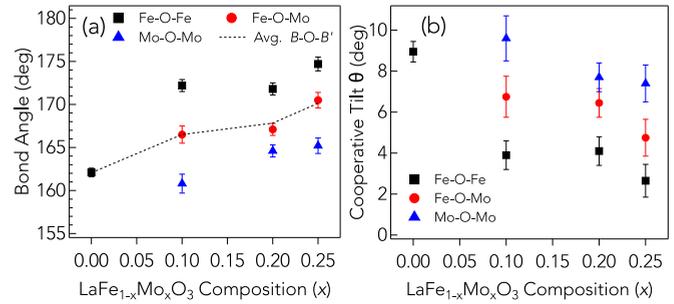

FIG. 8. (a) Bond angles for both Fe and Mo measured by EXAFS. By increasing site substitution by Mo, the Fe-O-Fe bond angle relaxes and continuously increases as a function of doping. (b) The cooperative tilting of the octahedra is also reduced by increases in Mo doping.

overlap with oxygen p_π orbitals that produce a strong antiferromagnetic exchange [47]. The increase in TM-O-TM angle and the concomitant increase in d-d hopping should correspond to an increase in the bandwidth and antiferromagnetic exchange. Both insulating and metallic compounds maintain the same crystal structure and preserve their symmetry.

In order to understand the change in the strength of the on-site Coulomb interaction strength in going from LaFeO$_3$ to LaMoO$_3$, we have computed the values of bare and partially screened Coulomb interaction (v and U) within the constrained random-phase approximation (cRPA) [48–57] as implemented in the WIEN2K code [58] (for technical details see Supplemental Material [27]). The results of our calculations (see Table S3 in the Supplemental Material [27]) show that this method yielded a $U = 4.41$ eV for the $3d$ states in LaFeO$_3$, and $U = 2.37$ eV for the $4d$ states in LaMoO$_3$. Significantly, these values would clearly suggest an appreciable decrease of about 2.0 eV in the calculated strength of U in going from the $3d$ to $4d$ states. In addition, basic electronic structure (see Supplemental Material [27]) also indicates d-bandwidth (W) enhancement from around 4 to 6 eV upon going from $3d$ states in LaFeO$_3$ to $4d$ states in LaMoO$_3$, respectively. The behavior of correlated systems depends on a delicate balance between the band energy and the effective interaction of the correlated electrons. In the present case, U/W approximately changes from 1.1 to 0.4, indicating a 63% decrement for the $4d$ states compared to the $3d$ states. Therefore, our theoretical calculations clearly indicate that the one-electron bandwidth W of the $4d$ states in the $x = 0.25$ sample would be large, and with that, the ratio of the on-site Coulomb repulsion U to W is less than the critical value $(U/W)_c$, which is likely to favor a metallic phase.

V. CONCLUSIONS

A combined x-ray spectroscopic investigation was used to reveal a detailed picture of the evolution of electronic structure across the insulator-to-metal transition in LaFe$_{1-x}$Mo$_x$O$_3$. Our RPES valence band data suggest that states occurring at the E_F are due entirely to itinerant Mo $4d$ states for the $x = 0.25$ sample. The addition of delocalized Mo d states and Mo-O hybridization is likely to increase the effective bandwidth necessary for itinerant character in the

metallic sample. RPES taken across the Fe L_3 edge suggests different spectral contributions at the edge of the valence band stemming from two different Fe sites present in the metallic $LaFe_{1-x}Mo_xO_3$ ($x = 0.2$ and 0.25) compound. RIXS spectra taken at the Fe L edge for doped and undoped samples show strong electron correlation (U) for all three compounds, with d-d and charge-transfer features that are well resolved. The electron-doped metallic compound, with Mo concentration at $x = 0.25$, shows broad spectral structures that are associated with a metallic state and are evidence for closing of the insulating gap. The wide bandwidth low-energy structure in the RIXS spectra evidences both Fe inter- and intrasite excitations (between the charge ordered Fe sites) as well as possible *intersite* Fe-Mo excitations. These results show a suppression of itinerant electron behavior and the corresponding relevance of the localized electron picture for the Fe sites in all compounds. The Fe-O hybridization strength as shown through photoemission experiments is likely to maintain the AFM ordering present in the metallic sample. This balance between U and W lies in an intermediate range of interaction strengths in $LaFe_{0.75}Mo_{0.25}O_3$ to be simultaneously AFM and metallic.

[1] M. Imada, A. Fujimori, and Y. Tokura, Rev. Mod. Phys. **70**, 1039 (1998).

[2] M. B. Salamon and M. Jaime, Rev. Mod. Phys. **73**, 583 (2001).

[3] J. Q. Li, Y. Matsui, S. K. Park, and Y. Tokura, Phys. Rev. Lett. **79**, 297 (1997).

[4] C. N. R. Rao and A. Arulraj, Curr. Opin. Solid State Mater. Sci. **3**, 23 (1998).

[5] N. P. Armitage, P. Fournier, and R. L. Greene, Rev. Mod. Phys. **82**, 2421 (2010).

[6] M. Coey, Nature **430**, 155 (2004).

[7] D. V. Efremov, J. Van Den Brink, and D. I. Khomskii, Nat. Mater. **3**, 853 (2004).

[8] A. Cammarata and J. M. Rondinelli, Appl. Phys. Lett. **108**, 213109 (2016).

[9] P. Limelette, A. Georges, D. Jérome, P. Wzietek, P. Metcalf, and J. M. Honig, Science **302**, 89 (2003).

[10] S. K. Pandey, P. Mahadevan, and D. D. Sarma, Europhys. Lett. **117**, 57003 (2017).

[11] J. Zaanen, G. A. Sawatzky, and J. W. Allen, Phys. Rev. Lett. **55**, 418 (1985).

[12] S. Jana, S. K. Panda, D. Phuyal, B. Pal, S. Mukherjee, A. Dutta, P. A. Kumar, D. Hedlund, J. Schött, P. Thunström, Y. Kvashnin, H. Rensmo, M. V. Kamalakar, C. U. Segre, P. Svedlindh, K. Gunnarsson, S. Biermann, O. Eriksson, O. Karis, and D. D. Sarma, Phys. Rev. B **99**, 075106 (2019).

[13] M. Medarde, C. Dallera, M. Grioni, B. Delley, F. Vernay, J. Mesot, M. Sikora, J. A. Alonso, and M. J. Martínez-Lope, Phys. Rev. B **80**, 245105 (2009).

[14] J. Shi, Y. Zhou, and S. Ramanathan, Nat. Commun. **5**, 4860 (2014).

[15] S. Johnston, A. Mukherjee, I. Elfimov, M. Berciu, and G. A. Sawatzky, Phys. Rev. Lett. **112**, 106404 (2014).

[16] V. Bisogni, S. Catalano, R. J. Green, M. Gibert, R. Scherwitzl, Y. Huang, V. N. Strocov, P. Zubko, S. Balandeh, J. M. Triscone, G. Sawatzky, and T. Schmitt, Nat. Commun. **7**, 1 (2016).

[17] M. Reehuis, C. Ulrich, A. Maljuk, C. Niedermayer, B. Ouladdiaf, A. Hoser, T. Hofmann, and B. Keimer, Phys. Rev. B **85**, 184109 (2012).

[18] J. Herrero-Martin, G. Subias, J. Garcia, J. Blasco, and M. Concepción Sánchez, Phys. Rev. B **79**, 045121 (2009).

[19] S. J. Oh, J. W. Allen, I. Lindau, and J. C. Mikkelsen, Phys. Rev. B **26**, 4845 (1982).

[20] L. H. Tjeng, C. T. Chen, J. Ghijsen, P. Rudolf, and F. Sette, Phys. Rev. Lett. **67**, 501 (1991).

[21] L. Simonelli, C. Marini, W. Olszewski, M. Ávila Pérez, N. Ramanan, G. Guilera, V. Cuartero, and K. Klementiev, Cogent Phys. **3**, 1 (2016).

[22] A. Kotani and S. Shin, Rev. Mod. Phys. **73**, 203 (2001).

[23] L. J. P. Ament, M. van Veenendaal, T. P. Devereaux, J. P. Hill, and J. van den Brink, Rev. Mod. Phys. **83**, 705 (2011).

[24] K. Ishii, T. Tohyama, and J. Mizuki, J. Phys. Soc. Jpn. **82**, 021105 (2013).

[25] B. Ravel and M. Newville, J. Synchrotron Radiat. **12**, 537 (2005).

[26] S. I. Zabinsky, J. J. Rehr, A. Ankudinov, R. C. Albers, and M. J. Eller, Phys. Rev. B **52**, 2995 (1995).

[27] See Supplemental Material at http://link.aps.org/supplemental/10.1103/PhysRevMaterials.4.034405 for details for EXAFS analysis fits and parameters used, and technical details for Hubbard U calculations.

[28] H. Wadati, D. Kobayashi, H. Kumigashira, K. Okazaki, T. Mizokawa, A. Fujimori, K. Horiba, M. Oshima, N. Hamada, M. Lippmaa, M. Kawasaki, and H. Koinuma, Phys. Rev. B **71**, 035108 (2005).

[29] J. E. Kleibeuker, Z. Zhong, H. Nishikawa, J. Gabel, A. Müller, F. Pfaff, M. Sing, K. Held, R. Claessen, G. Koster, and G. Rijnders, Phys. Rev. Lett. **113**, 237402 (2014).

[30] M. Besse, V. Cros, A. Barthélémy, H. Jaffrès, J. Vogel, F. Petroff, A. Mirone, A. Tagliaferri, P. Bencok, P. Decorse, P. Berthet, Z. Szotek, W. M. Temmerman, S. S. Dhesi, N. B. Brookes, A. Rogalev, and A. Fert, Europhys. Lett. **60**, 608 (2002).

[31] V. Kanchana, G. Vaitheeswaran, M. Alouani, and A. Delin, Phys. Rev. B **75**, 220404(R) (2007).

[32] J.-S. Kang, H. Han, B. W. Lee, C. G. Olson, S. W. Han, K. H. Kim, J. I. Jeong, J. H. Park, and B. I. Min, Phys. Rev. B **64**, 024429 (2001).

[33] R. Thomas, J. Kas, P. Glatzel, M. Al Samarai, F. M. F. De Groot, R. Alonso Mori, M. Kavčič, M. Zitnik, K. Bucar, J. J. Rehr, and M. Tromp, J. Phys. Chem. C **119**, 2419 (2015).

[34] Z. Cui, X. Zhai, Y. D. Chuang, H. Xu, H. Huang, J. Wang, Z. Fu, R. Peng, J. Guo, and Y. Lu, Phys. Rev. B **95**, 205102 (2017).

[35] T. Nomura, Y. Harada, H. Niwa, K. Ishii, M. Ishikado, S. Shamoto, and I. Jarrige, Phys. Rev. B **94**, 035134 (2016).

[36] C. Monney, A. Uldry, K. J. Zhou, A. Krzton-Maziopa, E. Pomjakushina, V. N. Strocov, B. Delley, and T. Schmitt, Phys. Rev. B **88**, 165103 (2013).

[37] S. M. Butorin, J. Electron Spectrosc. Relat. Phenom. **110**, 213 (2000).

[38] D. E. McNally, X. Lu, J. Pelliciari, S. Beck, M. Dantz, M. Naamneh, T. Shang, M. Medarde, C. W. Schneider, V. N. Strocov, E. V. Pomjakushina, C. Ederer, M. Radovic, and T. Schmitt, npj Quantum Mater. **4**, 1 (2019).

[39] C. Monney, K. J. Zhou, H. Cercellier, Z. Vydrova, M. G. Garnier, G. Monney, V. N. Strocov, H. Berger, H. Beck, T. Schmitt, and P. Aebi, Phys. Rev. Lett. **109**, 047401 (2012).

[40] K. Ishii, T. Inami, K. Ohwada, K. Kuzushita, J. Mizuki, Y. Murakami, S. Ishihara, Y. Endoh, S. Maekawa, K. Hirota, and Y. Moritomo, Phys. Rev. B **70**, 224437 (2004).

[41] S. Grenier, J. P. Hill, V. Kiryukhin, W. Ku, Y. J. Kim, K. J. Thomas, S. W. Cheong, Y. Tokura, Y. Tomioka, D. Casa, and T. Gog, Phys. Rev. Lett. **94**, 047203 (2005).

[42] A. Agui, T. Uozumi, M. Mizumaki, and T. Käämbre, Phys. Rev. B **79**, 092402 (2009).

[43] J. M. Chen, J. M. Lee, S. W. Huang, K. T. Lu, H. T. Jeng, C. K. Chen, S. C. Haw, T. L. Chou, S. A. Chen, N. Hiraoka,

[44] T. Berlijn, P. C. Snijders, O. Delaire, H.-D. Zhou, T. A. Maier, H.-B. Cao, S.-X. Chi, M. Matsuda, Y. Wang, M. R. Koehler, P. R. C. Kent, and H. H. Weitering, Phys. Rev. Lett. **118**, 077201 (2017).

[45] J. Matsuno, T. Mizokawa, A. Fujimori, Y. Takeda, S. Kawasaki, and M. Takano, Phys. Rev. B **66**, 193103 (2002).

[46] T. Moriya and Y. Takahashi, Annu. Rev. Mater. Sci. **14**, 1 (1984).

[47] D. I. Khomskii, *Transition Metal Compounds* (Cambridge University Press, Cambridge, 2014).

[48] F. Aryasetiawan, M. Imada, A. Georges, G. Kotliar, S. Biermann, and A. I. Lichtenstein, Phys. Rev. B **70**, 195104 (2004).

[49] L. Vaugier, H. Jiang, and S. Biermann, Phys. Rev. B **86**, 165105 (2012).

[50] G. Kresse and J. Hafner, Phys. Rev. B **47**, 558 (1993).

[51] P. E. Blöchl, Phys. Rev. B **50**, 17953 (1994).

[52] C. Martins, M. Aichhorn, L. Vaugier, and S. Biermann, Phys. Rev. Lett. **107**, 266404 (2011).

[53] Y. Nomura, M. Kaltak, K. Nakamura, C. Taranto, S. Sakai, A. Toschi, R. Arita, K. Held, G. Kresse, and M. Imada, Phys. Rev. B **86**, 085117 (2012).

[54] S. K. Panda, I. Dasgupta, E. Şaşoğlu, S. Blugel, and D. D. Sarma, Sci. Rep. **3**, 2995 (2013).

[55] B. Amadon, T. Applencourt, and F. Bruneval, Phys. Rev. B **89**, 125110 (2014).

[56] A. van Roekeghem, L. Vaugier, H. Jiang, and S. Biermann, Phys. Rev. B **94**, 125147 (2016).

[57] S. K. Panda, H. Jiang, and S. Biermann, Phys. Rev. B **96**, 045137 (2017).

[58] K. Schwarz and P. Blaha, Comput. Mater. Sci. **28**, 259 (2003).